Pressure drop across wire mesh demister in desalination plants using Eulerian–Eulerian modeling and computational fluid dynamics simulation

Danah Al-Rabiah*, Hala Al-Fulaij, Hisham Ettouney

Department of Chemical Engineering, College of Engineering and Petroleum, Kuwait University, P.O. Box 5969, Safat 13060, Kuwait, emails: danah_r@yahoo.com (D. Al-Rabiah), engrhala@yahoo.com (H. Al-Fulaij), ettouney@hotmail.com (H. Ettouney)

ABSTRACT

This study focuses on the development of design correlation for pressure drop in wire mesh demisters, used in the multistage flash desalination process (MSF) as well as similar evaporation and flashing units found in other industrial processes. Development of the correlation is based on numerical simulation of the demister using steady-state and two-dimensional model for the flow of vapor and brine droplets through the demister. An Eulerian model was used to model the system and the resulting model equations were solved using a commercial computational fluid dynamics software (FLUENT). The system model was formed of three zones, which include the vapor space above and below the demister and the demister. In addition, the demister was approximated as a porous media. A sensitivity analysis of the model revealed that vapor velocity, demister packing density and height, and the inlet flashed-off vapor composition are the main parameters that affect demister performance. Consequently, numerical data were used to correlate pressure drop across the demister as a function of operating and design parameters. The developed correlation was validated using data from real MSF plants. Analysis indicated that the correlation predictions and experimental data were consistent and showed good agreement with an error less than 25%.

Keywords: Desalination; Eulerian modeling; Multistage flashing; CFD; Demister

1. Introduction

A demister is a simple porous blanket of metal or plastic wire used in vapor–liquid separators, vessels such as distillation column, absorber, and evaporator. In multistage flash desalination process (MSF), demister is a very important part, it effects the purification of distilled water by removing entrained brine droplets from flashed-off vapor and prevents formation of scale on tube bundle in the flashing chamber. It is desired to have a low pressure drop, high mist removal efficiency, and low cost. The performance of the demister depends on many design parameters such as wire diameter, supporting grids, packing density, pad thickness, material of construction, and vapor velocity [1].

A limited number of studies were made on modeling of the demister. El-Dessouky et al. [2] predicted a correlation for the droplet separation efficiency as a function of vapor velocity based on experimental data. Buerkholz [3] found that when the vapor velocity within the demister is 4–5 m/s, no water droplets will re-entrain in wire-mesh pad. Ettouney [4] studied brine re-entrainment from the demister in the winter

*Corresponding author.

season due to the reduction in the intake seawater temperature that can be controlled using either an RO system to reduce the salinity of inlet water or use of product water generated in the first few stages.

Gharib and Moraveji [5], working on vane demisters using computational fluid dynamics (CFD) modeling, found that minimizing the plate spacing led to a rise in the efficiency of droplet collection to 99.4% with an increase in the pressure drop. Venkatesane et al. [6] used a two-dimensional CFD model to simulate flow in curved vanes. The simulation validated the predictions of various flow models against experimental measurements. Analysis showed that several of the used models gave excellent predictions of the measurements. Venkatesane et al. [7] found the numerically predicted vane separation efficiency range was between 99.2 and 99.4% using CFD. Venkatesane et al. [8] discussed the base design of the carved vane demister geometry with multiple parameters and levels using the Taguchi-based approach to select an orthogonal array of 25 designs.

Al-Fulaij et al. [9] focused on CFD modeling of demisters and found that choosing 0.24-mm-diameter wire will reduce pressure drop without affecting separation efficiency, but will reduce the required heat transfer area and as a result will reduce the plant capital cost. Rahimi and Abbaspour [10] predicted a correlation for pressure drop in the demister using CFD and compared the results with the experimental and empirical correlations of El-Dessouky et al. [2]. The results showed 21% deviation from the empirical model. Galletti et al. [11] used CFD to develop a two-dimensional Eulerian/Lagrangian model of two wave-plate mist eliminators, both equipped with drainage channels. Predictions have been compared with comprehensive experimental data on removal efficiency for both eliminators. Zhao et al. [12] used CFD to develop a two-dimensional Eulerian/Lagrangian model of demister vane with various geometries and operating conditions based on response surface methodology. Kouhikamali et al. [13] studied the effect of geometry and operating conditions on the pressure drop and separation efficiency of wire mesh mist eliminator numerically. Their results showed that the separation efficiency increases with an increase in the droplet size, packing thickness, packing density, and vapor velocity and decreases with a decrease in the wire diameter. Also they concluded that the maximum separation efficiency was obtained with a vapor velocity range of 8–10 m/s.

In this study, an Eulerian–Eulerian model is used to perform the sensitivity analysis of demister performance to study the effects of major operating/design parameters such as vapor velocity, packing density,

inlet droplet fraction, and face permeability on the pressure drop across the wire mesh demister. Also a new correlation for the pressure drop across the demister is predicted, compared against other correlation, and validated against real plant data and El-Dessouky et al. [2] experimental data.

2. Model assumptions

The computational domain is shown in Fig. 1, and it includes three zones, which are the vapor space below the demister, the demister, and the vapor space above the demister. The following assumptions are invoked in model development:

(1) The Eulerian–Eulerian approach: the vapor phase and brine droplets are both modeled by the Eulerian model. This approach models both phases as two separate continuums. Accordingly, the model equations for each phase are solved simultaneously.
(2) The porous media approximation: the demister is simulated as a porous media. The porous media assumption is invoked because the MSF wire mesh demisters have a porosity varying between 80 and 99% and the demister has a uniform distribution of void and wire volumes.
(3) Two-dimensional computational domain: the dimensions of the MSF demister are in the ranges of 0.8–1.6 m, 0.15–0.5 m, and 0.1–0.25 m in length (z-direction), width (x-direction), and height (y-direction), respectively. As shown in Fig. 1, only the x and y directions are
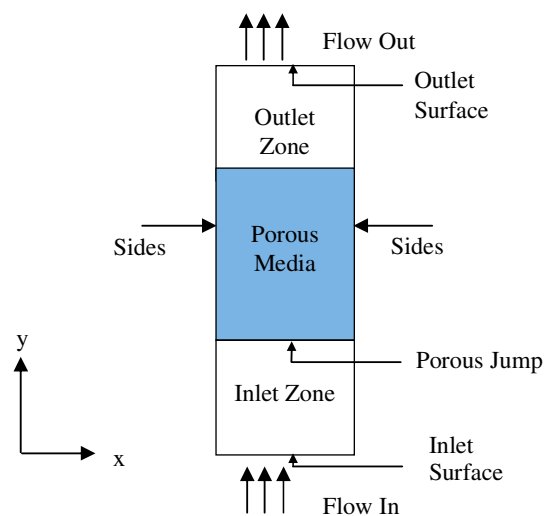
Fig. 1. Schematic diagram of the porous media approach.

considered in the simulation. This is because as the vapor flows upward in the y-direction, the vapor will bend around the demister wires in the x-direction and it is assumed that this flow pattern is symmetric in the z-direction along the demister length. The computational domain was limited to the entire height of the demister and a width of 0.03 m. Selection of the optimum value of this width was arrived at using several numerical tests in order to eliminate end effects on the vapor flow and the resulting separation efficiency and pressure drop. The remainder of the computational domain includes the vapor space below and above the demister. The height of either domain was limited to a value of 0.15 m, which was tested to eliminate end effects on the vapor flow below and above the demister.

(4) Constant mass sink for brine droplets: the value of the constant mass sink for the brine droplets is set according to the removal efficiency. This assumption was invoked to prevent accumulation of the brine droplets within the demister. In actual operation, the brine droplets attached to the demister wires increase in size and mass and subsequently fall back into the brine pool due to gravitational effects. Use of the constant mass sink requires knowledge of the separation efficiency of the demister, which usually has values above 98%. This assumption can be eliminated if the brine droplets are modeled by the Lagrangian model, where a brine droplet can be removed once it reaches the wire boundary [14].

(5) Equal pressure and temperature in water vapor and brine droplets: this assumption implies that the vapor and brine droplets have the same pressure and temperature. This assumption is valid because of the small fraction of the brine droplets in the vapor phase. Also, the size of the brine droplets is small, which provides a large surface area for heat transfer between the brine droplets and the vapor. Subsequently, both phases will have the same temperature and in turn there will be no heat transfer between the two phases.

(6) The Schmidt number is equal to one: this is made by setting the turbulent diffusivity equal to the turbulent viscosity, which implies equality of the rates of viscous diffusion and mass diffusion. This condition is valid for dilute gaseous [15], which is the case for the mixture of brine droplets and water vapor.

3. Model equations

This section includes details of the model equations for the two-dimensional Eulerian scheme of vapor and brine droplet flow through the demister, which is assumed to be a porous media. The model equations include conservation of mass and conservation of momentum.

3.1. Conservation of mass

Equations for mass conservation are developed after the study by Zikanov [16]. These equations are time dependent, two dimensional, and have a constant density. The conservation of mass of the vapor phases is:

$$\rho_g \left[\frac{\partial \psi_g}{\partial t} + \frac{\partial}{\partial x}\left(\psi_g u_g \right) + \frac{\partial}{\partial y}\left(\psi_g v_g \right) \right] = 0 \tag{1}$$

The conservation of mass of the brine droplets is:

$$\rho_l \left[\frac{\partial \psi_l}{\partial t} + \frac{\partial}{\partial x}\left(\psi_l u_l \right) + \frac{\partial}{\partial y}\left(\psi_l v_l \right) \right] = -\psi_l \dot{m} \tag{2}$$

The porosity of the demister is:

$$\omega = \psi_g + \psi_l \tag{3}$$

where the porosity ω is the volume of voids over the total volume, u is the velocity in the x-direction, v is the velocity in the y-direction, $\dot{m}$ is the mass rate of collected liquid droplets per unit volume, and ψ is the volume fraction.

3.2. Conservation of momentum

The model equations for conservation of momentum of the vapor phase in two-dimensional model (x-direction, horizontal and y-direction, vertical) are developed after the study by Hu and Zhang [17]:

$$\begin{aligned}
\frac{\partial (\psi_g \rho_g u_g)}{\partial t} &+ \frac{\partial}{\partial x}\left(\psi_g \rho_g u_g u_g \right) + \frac{\partial}{\partial y}\left(\psi_g \rho_g v_g u_g \right) \\
&= \frac{\partial}{\partial x}\left(\psi_g \mu_{eg} \frac{\partial u_g}{\partial x} \right) + \frac{\partial}{\partial y}\left(\psi_g \mu_{eg} \frac{\partial u_g}{\partial y} \right) + \frac{\partial}{\partial x}\left(\psi_g \mu_{eg} \frac{\partial u_g}{\partial x} \right) \\
&+ \frac{\partial}{\partial y}\left(\psi_g \mu_{eg} \frac{\partial v_g}{\partial x} \right) - \frac{2}{3}\frac{\partial}{\partial x}\left[\psi_g \mu_{eg} \left(\frac{\partial u_g}{\partial x} + \frac{\partial v_g}{\partial y} \right) \right] \\
&- \psi_g \frac{\partial P}{\partial x} + S_{gx} - R_{gx}
\end{aligned} \tag{4}$$

$$\frac{\partial\left(\psi_g\rho_g v_g\right)}{\partial t}+\frac{\partial}{\partial x}\left(\psi_g\rho_g u_g v_g\right)+\frac{\partial}{\partial y}\left(\psi_g\rho_g v_g v_g\right)$$
$$=\frac{\partial}{\partial x}\left(\psi_g\mu_{eg}\frac{\partial v_g}{\partial x}\right)+\frac{\partial}{\partial y}\left(\psi_g\mu_{eg}\frac{\partial v_g}{\partial y}\right)+\frac{\partial}{\partial x}\left(\psi_g\mu_{eg}\frac{\partial u_g}{\partial y}\right)$$
$$+\frac{\partial}{\partial y}\left(\psi_g\mu_{eg}\frac{\partial v_g}{\partial y}\right)-\frac{2}{3}\frac{\partial}{\partial y}\left[\psi_g\mu_{eg}\left(\frac{\partial u_g}{\partial x}+\frac{\partial v_g}{\partial y}\right)\right]$$
$$-\psi_g\frac{\partial P}{\partial y}+S_{gy}-R_{gy}$$

$$(5)$$

On the left-hand side of Eqs. (4) and (5), the first term represents the transient unsteady acceleration and the second and third terms represent the convective acceleration. On the right-hand side, the first five terms represent the viscous terms (shear stress described by Newtonian closure) and the sixth term represents the pressure gradient due to buoyancy. The source term due to interfacial friction between the gas phase and the liquid phase is S, and the source term due to the distributed resistance, which is attributed to the tube bundle, is R. The effective viscosity is μ_{eg}, which is the sum of the turbulent viscosity, μ_{t_g}. The fluid viscosity is μ_g.

The equations for the conservation of momentum for brine droplets are developed after the study by Al-Fulaij [18]:

$$\frac{\partial(\psi_l\rho_l u_l)}{\partial t}+\frac{\partial}{\partial x}(\psi_l\rho_l u_l u_l)+\frac{\partial}{\partial y}(\psi_l\rho_l v_l u_l)$$
$$=-\psi_l\frac{\partial P}{\partial x}+S_{lx}-R_{lx}-\psi_l\dot{m}u_l$$

$$(6)$$

$$\frac{\partial(\psi_l\rho_l v_l)}{\partial t}+\frac{\partial}{\partial x}(\psi_l\rho_l u_l v_l)+\frac{\partial}{\partial y}(\psi_l\rho_l v_l v_l)$$
$$=-\psi_l\frac{\partial P}{\partial y}+S_{ly}-R_{ly}-\psi_l\dot{m}v_l+\psi_l\rho_l g$$

$$(7)$$

3.3. Interfacial friction

From the momentum equation, the interfacial friction forces between the vapor and the brine droplets are related to the interfacial friction coefficient, C_f, which is given as [19]:

$$C_{f_u}=\frac{1}{2}\rho_g f_d A_{do}\left|u_g-u_l\right|$$

$$(8)$$

$$C_{f_v}=\frac{1}{2}\rho_g f_d A_{do}\left|v_g-v_l\right|$$

$$(9)$$

where f_d is the friction factor for spherical objects that is obtained from an empirical correlation given by Clift et al. [20], and A_{do} is the total projected area of droplets in a given control volume that is defined as:

$$A_{do}=\frac{1.5\psi_l V}{D_{do}}$$

$$(10)$$

From the momentum equations, the interfacial friction forces between the gas and liquid phases are developed after the study by Hu and Zhang [17]:

$$S_{gx}=-S_{lx}=C_{f_u}(u_l-u_g)$$

$$(11)$$

$$S_{gy}=-S_{ly}=C_{f_v}(v_l-v_g)$$

$$(12)$$

3.4. Distributed resistance

The source term for the distributed resistance (local hydraulic resistance) due to the tube bundles for both phases (liquid and gas) is included in the momentum equations [9].

For the liquid phase in the *x*-direction:

$$R_{lx}=(\psi_l\xi_{lx}\rho_l u_l U_l)$$

$$(13)$$

For the liquid phase in the *y*-direction:

$$R_{ly}=\left(\psi_l\xi_{ly}\rho_l v_l U_l\right)$$

$$(14)$$

For the vapor phase in the *x*-direction:

$$R_{gx}=\left(\psi_g\xi_{gx}\rho_g u_g U_g\right)$$

$$(15)$$

For the vapor phase in the *y*-direction:

$$R_{gy}=\left(\psi_g\xi_{gy}\rho_g v_g U_g\right)$$

$$(16)$$

where ξ is the pressure loss coefficient. The expression for the x and y directions is given by [21]:

$$\xi_x=2\left(\frac{f_x}{P_t}\right)\left(\frac{P_t\omega}{P_t-D_{ot}}\right)^2\left(\frac{1-\omega}{1-\omega_{td}}\right)$$

$$(17)$$

$$\xi_y=2\left(\frac{f_y}{P_t}\right)\left(\frac{P_t\omega}{P_t-D_{ot}}\right)^2\left(\frac{1-\omega}{1-\omega_{td}}\right)$$

$$(18)$$

where

$$
f_x = \begin{cases} 0.619 Re_x^{-0.198}; & Re_x < 8000 \\ 1.156 Re_x^{-0.2647}; & 8000 \leq Re_x < 2 \times 10^5 \end{cases} \tag{19}
$$

$$
f_y = \begin{cases} 0.619 Re_y^{-0.198}; & Re_y < 8000 \\ 1.156 Re_y^{-0.2647}; & 8000 \leq Re_y < 2 \times 10^5 \end{cases} \tag{20}
$$

3.5. Mass source term

The mass source term $\dot{m}$ is the total mass of the collected entrained brine droplets. The collection takes place on the wires, as mentioned previously. For simplification, $\dot{m}$ is assumed to be constant and equal to a percentage of the inlet liquid flow rate, depending on the demister separation efficiency. For this model, a uniform mass sink distribution is assumed for water droplets across the demister fluid zone in both approaches (tube bank and porous media).

3.6. Turbulence model

The standard k–ε model was used for all simulations in this study. This model uses two differential equations: turbulent kinetic energy, k, and turbulent dissipation rate, ε. For the gas phase, the model has the following form [18]:

$$
\begin{aligned}
&\frac{\partial}{\partial t}\left(\psi_g \rho_g k_g\right) + \frac{\partial}{\partial x}\left(\psi_g \rho_g u_g k_g\right) + \frac{\partial}{\partial y}\left(\psi_g \rho_g v_g k_g\right) \\
&= \frac{\partial}{\partial x}\left(\psi_g\left(\mu_g + \frac{\mu_{t_g}}{\sigma_k}\right)\frac{\partial k_g}{\partial x}\right) + \frac{\partial}{\partial y}\left(\psi_g\left(\mu_g + \frac{\mu_{t_g}}{\sigma_k}\right)\frac{\partial k_g}{\partial y}\right) \\
&\quad + \psi_g(G_g - \rho_g \varepsilon_g) + S_{k_g}
\end{aligned} \tag{21}
$$

$$
\begin{aligned}
&\frac{\partial}{\partial t}\left(\psi_g \rho_g \varepsilon_g\right) + \frac{\partial}{\partial x}\left(\psi_g \rho_g u_g \varepsilon_g\right) + \frac{\partial}{\partial y}\left(\psi_g \rho_g v_g \varepsilon_g\right) \\
&= \frac{\partial}{\partial x}\left(\psi_g\left(\mu_g + \frac{\mu_{t_g}}{\sigma_k}\right)\frac{\partial \varepsilon_g}{\partial x}\right) + \frac{\partial}{\partial y}\left(\psi_g\left(\mu_g + \frac{\mu_{t_g}}{\sigma_k}\right)\frac{\partial \varepsilon_g}{\partial y}\right) \\
&\quad + \psi_g \frac{\varepsilon_g}{k_g}\left(C_1 G_g - C_2 \rho_g \varepsilon_g\right) + S_{\varepsilon_g}
\end{aligned} \tag{22}
$$

For the liquid phase, the model has the following form:

$$
\begin{aligned}
&\frac{\partial}{\partial t}(\psi_l \rho_l k_l) + \frac{\partial}{\partial x}(\psi_l \rho_l u_l k_l) + \frac{\partial}{\partial y}(\psi_l \rho_l v_l k_l) \\
&= \frac{\partial}{\partial x}\left(\psi_l\left(\mu_l + \frac{\mu_{t_l}}{\sigma_k}\right)\frac{\partial k_l}{\partial x}\right) + \frac{\partial}{\partial y}\left(\psi_l\left(\mu_l + \frac{\mu_{t_l}}{\sigma_k}\right)\frac{\partial k_l}{\partial y}\right) \\
&\quad + \psi_l(G_l - \rho_l \varepsilon_l) + S_{k_l}
\end{aligned} \tag{23}
$$

$$
\begin{aligned}
&\frac{\partial}{\partial t}(\psi_l \rho_l \varepsilon_l) + \frac{\partial}{\partial x}(\psi_l \rho_l u_l \varepsilon_l) + \frac{\partial}{\partial y}(\psi_l \rho_l v_l \varepsilon_l) \\
&= \frac{\partial}{\partial x}\left(\psi_l\left(\mu_l + \frac{\mu_{t_l}}{\sigma_k}\right)\frac{\partial \varepsilon_l}{\partial x}\right) \\
&\quad + \frac{\partial}{\partial y}\left(\psi_l\left(\mu_l + \frac{\mu_{t_l}}{\sigma_k}\right)\frac{\partial \varepsilon_l}{\partial y}\right)\psi_l \frac{\varepsilon_l}{k_l}\left(C_1 G_l - C_2 \rho_l \varepsilon_l\right) + S_{\varepsilon_l}
\end{aligned} \tag{24}
$$

where μ_{t_g} is the turbulent viscosity of the gas phase and is defined as:

$$
\mu_{t_g} = \frac{C_\mu \rho_g k_g^2}{\varepsilon_g} \tag{25}
$$

The turbulent viscosity of the liquid phase, μ_{t_l}, is defined as [10]:

$$
\mu_{t_l} = \frac{C_\mu \rho_l k_l^2}{\varepsilon_l} \tag{26}
$$

The standard turbulence model, without any modifications, was used with standard wall functions. The source terms S_k and S were not considered in determining the mean of interfacial turbulence exchange [10]. The five constants of the model were set to the standard k–ε model values: $\sigma_k = 1$, $\sigma = 1.3$, $C_1 = 1.44$, $C_2 = 1.92$, and $C_\mu = 0.09$ ([10,17]).

4. Boundary conditions

The boundary conditions for the porous media approach include the fluid zone (including the porous media), flow inlet conditions, pressure outlet conditions, geometric symmetry, and porous jump boundary conditions at the inlet of the porous media. The porous jump model is applied to a face zone, not to a cell zone, and should be used (instead of the full porous media model) whenever possible because it is more robust and yields better convergence [22].

Flow inlet boundary condition is used to define the velocity and scalar properties of the flow at inlet boundaries. It is defined in the CFD code on the inlet surface as "velocity inlet". For this boundary condition, several parameters should be defined to perform the simulation including the velocity magnitude and direction or velocity components, temperature (for energy calculations), outflow gage pressure (for calculations with the density-based solvers), turbulence parameters (for turbulent calculations), mixture fraction and variance (for non-premixed or partially premixed combustion calculations), and multiphase boundary conditions (for general multiphase calculations).

Table 1
Input operating conditions and design parameters used for grid analysis in FLUENT code

	Lab-scale demister	Industrial-scale, high-temperature demister	Industrial-scale, low-temperature demister
Velocity range (m/s)	2.44	1.252	9.718
Packing density (kg/m^3)	80.317	80.317	80.317
Water droplet volume fraction in the inlet stream	7.34×10^{-5}	1.37×10^{-5}	3.78×10^{-5}
Droplet diameter	12 µm [26]	10 µm [25]	8 µm [25]
Porosity	0.9899	0.9899	0.9899
Temperature (K)	373.15	377.548	313.1

Pressure outlet boundary conditions are used to determine the static pressure at flow outlets (and also other scalar variables, in the case of backflow). It is defined in the CFD code on the outlet surface as "pressure outlet". The use of a pressure outlet boundary condition instead of an outflow condition often results in a better rate of convergence when backflow occurs during iteration. Also, it should be noticed that the outflow boundary condition which is more general cannot be used with multiphase model such as the model in this study. For this boundary condition, the static pressure and backflow conditions which include backflow direction specification method, turbulence parameters (for turbulent calculations), and multiphase boundary conditions (for general multiphase calculations) should be entered.

Symmetry boundary conditions are defined in the CFD code on both sides of the geometry as "symmetry". This condition is used when the physical geometry of interest, and the expected pattern of the flow/thermal solution, has mirror symmetry. FLUENT assumes a zero flux of all quantities across a symmetry boundary. There is no convective flux across a symmetry plane: the normal velocity component at the symmetry plane is thus zero. There is no diffusion flux across a symmetry plane: the normal gradients of all flow variables are thus zero at the symmetry plane. The symmetry boundary condition can therefore be summarized as zero normal velocity at a symmetry plane or zero normal gradients of all variables at a symmetry plane.

The middle zone which includes the demister is defined in the CFD code as "porous media". In this model, a cell zone in which the porous media model is applied is defined and the pressure loss in the flow is determined via the inputs. The following information is required to define a porous media boundary: define the porous zone, identify the fluid material flowing through the porous medium, enable the relative velocity resistance formulation (by default, this option is already enabled and takes the moving porous media into consideration), set the viscous resistance coefficients and the inertial resistance coefficients, and define the direction vectors for which they apply. Alternatively, specify the coefficients for the power-law model. Also, specify the porosity of the porous medium which was calculated from the packing density as:

$$\omega = 1 - \frac{\rho_w}{\rho_P} \tag{27}$$

It is optional to set any fixed values for solution variables in the fluid region. If appropriate, suppress the turbulent viscosity in the porous region.

Porous jump condition allows accounting for the pressure drop across the porous media. Porous jump conditions are used to model a thin membrane. In this case, it is the inlet of the porous media. For this boundary condition, the porous-jump zone should be identified, and the face permeability of the medium (δ), the porous medium thickness, and the pressure-jump coefficient C_2 were set. One technique for deriving the appropriate constants δ and C_2 involves the use of the Ergun equation [23]. In this technique, the porous media is treated as packed bed. Semiempirical correlation applicable over a wide range of Reynolds numbers and for many types of packing is given as follows:

$$\delta = \frac{D_{ot}^2}{150} \frac{\omega^3}{(1-\omega)^2} \tag{28}$$

$$C_2 = \frac{3.5}{D_{ot}} \frac{(1-\omega)}{w^3} \tag{29}$$

5. Solution method

The model was solved by finite approaches using a commercial CFD software package (FLUENT 6.3) based on the finite-volume approach. The multiphase flow model, which is based on the Eulerian–Eulerian

approach, utilizes a pressure-based solver that is suitable at low speeds and incompressible flows. The code adapted a finite-volume discretization scheme to convert the scalar transport equations into algebraic equations that could be solved numerically. To ensure convergence, we discretized in space through a first-order upwind scheme where cell-face quantities are determined by assuming that the cell-center values of any field variable represent cell averages that hold throughout the entire cell. Therefore, face quantities are identical to cell quantities and are set equal to the cell-center values in upstream cells (relative to the direction of the normal velocity) [24]. A review of previous literature studies by Hu and Zhang [17] and Rahimi and Abbaspour [10] shows that the use of the first-order upwind approximation provides results that accurately simulate different flow configurations, i.e., flow around condenser tubes and across a demister in a reactor.

The SIMPLE (Simultaneous Solution of Non-linearity Coupled Equations) algorithm was adopted to couple pressure and velocity. Under-relaxation factors of 0.3 were adopted for all the variables. All calculations were completed using a convergence factor of 1E−7 for all calculated variables (velocities, continuity, etc.).

6. Domain geometry and grid analysis

Gambit software was used to create the grids. GAMBIT contains three meshing schemes: Quad (includes quadrilateral mesh elements), Tri (includes triangular mesh elements), and Quad/Tri (composed primarily of quadrilateral mesh elements but includes triangular corner elements at user-specified locations). The quadratic element is known to provide high accuracy and rapid convergence [22] and thus a uniform grid size of quadratic elements was used for all zones (inlet, demister, and outlet) of the porous media model.

The grid analysis was performed to predict the minimum number of grids that should be used to obtain results that are independent of the grid size and results in less computational time. This was achieved by simulating identical geometries (demister), boundary conditions, and operating variables. The simulations were repeated for the conditions shown in Table 1, which included a laboratory-scale demister and an industrial-scale demister operating at both high and low temperatures. The simulations were based on a comparison of the calculated separation efficiency, pressure drop, and velocity (both x and y components). Sample results of the pressure drop grid analysis for the three cases given in Table 1

are shown in Fig. 2. As shown, the optimum number of grid cells for the porous media approach was 52,500 cells.

7. Model validation

The CFD FLUENT code was used to simulate demisters in the MSF process at both the laboratory
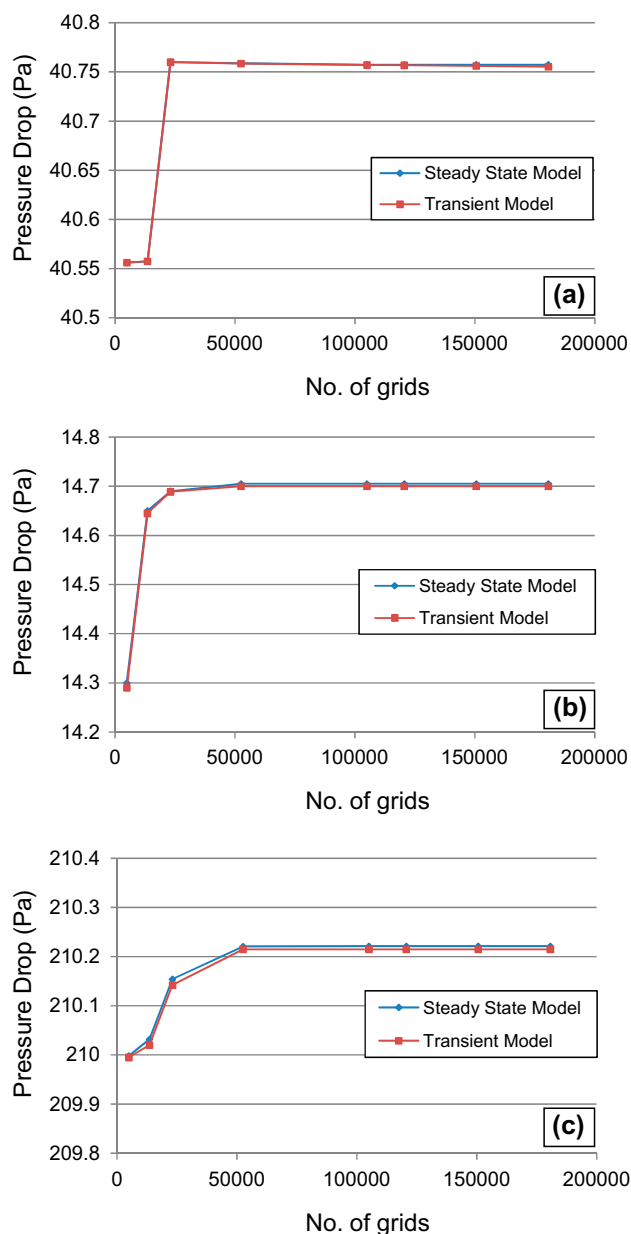
Fig. 2. Pressure drop values obtained for the porous media geometry with varying numbers of grid elements for (a) lab-scale demister, (b) high-temperature stage demister, and (c) low-temperature stage demister.

Table 2
Input operating conditions and design parameters for the FLUENT code

Velocity range (m/s)	1.13–12
Packing density (kg/m^3)	80.317, 120.5, 140.6, 176.35, 189, 208.16
Water droplet volume fraction in the inlet stream	4.9E−7 to 6.5E−5
Droplet diameter	10 μm = 10E−6 m
Porosity	Calculated for the packing density range of (0.78–0.9899)
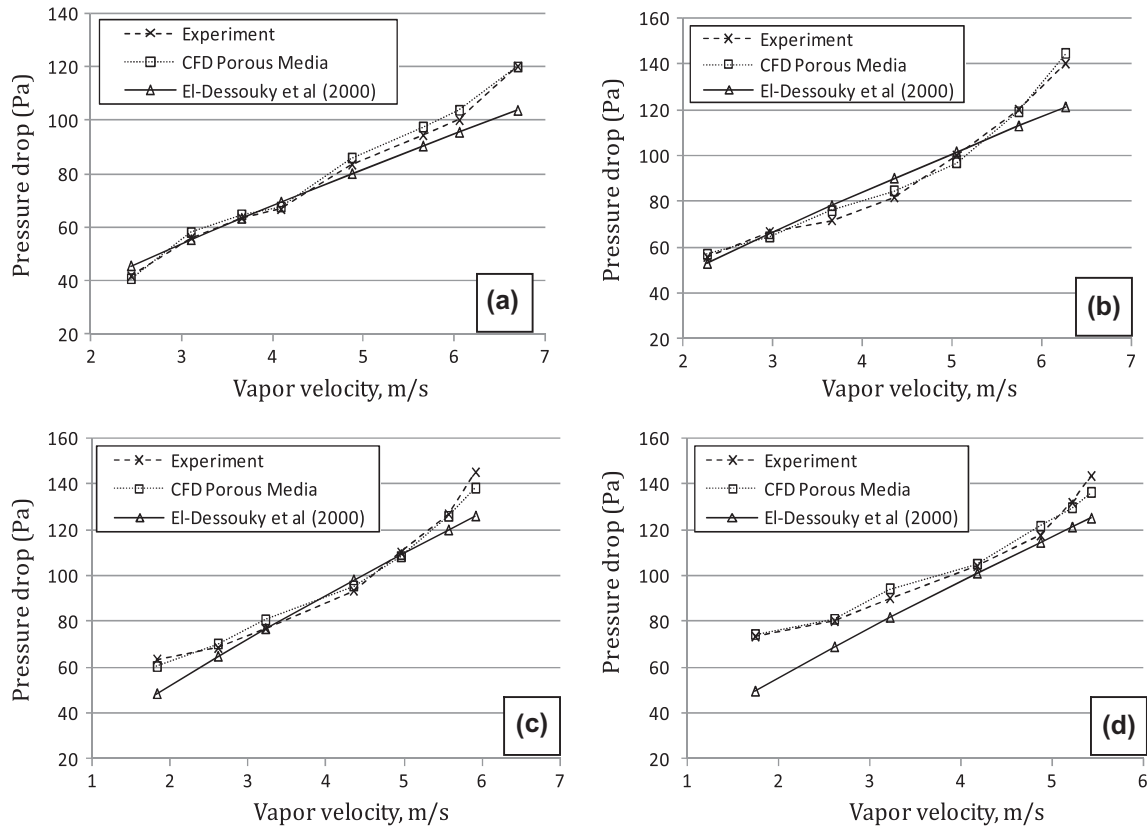
Fig. 3. Variation in pressure drop as a function of vapor velocity for a demister with a wire diameter = 0.28 mm and packing density of (a) 80.317 kg/m^3, (b) 140.6 kg/m^3, (c) 176.35 kg/m^3, and (d) 208.16 kg/m^3.

and industrial scales operating at both high and low temperatures. The use of different types of data was essential to demonstrate the generality of the model, which make the model more reliable. After validation, the model was used in a sensitivity analysis to predict the effect of various design and operating parameters on demister pressure drop.

The experiment was performed by El-Dessouky et al. [2] with an industrial demister. All experimental measurements gave average values for pressure drop and removal efficiency across the demister. There were no detailed measurements of either variable within the demister. All measurements were made under steady-state conditions. The ranges of the experimental vari-

ables were as follows: (1) vapor velocity (0.98–7.5 m/s), (2) packing density (80.317–208.16 kg/m3), (3) demister pad thickness (100–200 mm), (4) wire diameter (0.2–0.32 mm), and (5) droplet size (1–5 mm). It should be noted that the above experimental ranges vary from high to intermediate temperatures of industrial scale flashing stages. The error analysis of the experimental data gave errors of 2.4% for temperature, 3.15% for flow rate, 2.73% for pressure drop, 2.31% for absolute pressure, and 1.19% for liquid level. On the basis of these errors, the pressure drop of the wet demister, separation efficiency, and velocities for loading and flooding may deviate by 4.6, 3.2, and 4.1% from the true values [2]. Table 2 includes the operating

Table 3
Operating conditions for the flash stages of a MSF-BC plant at low temperatures

Stage	Vapor temperature below demister (K)	Vapor density (kg/m^3)	Droplet density (kg/m^3)	Flashed-off vapor velocity (m/s)	Inlet volume fraction of droplet in flashed-off vapor
1	361.690	0.417	1,013.3	1.829	3.181E−06
2	359.256	0.382	1,015.1	2.805	2.898E−06
3	356.852	0.350	1,016.8	3.006	2.638E−06
4	354.477	0.320	1,018.5	3.183	2.402E−06
5	352.131	0.293	1,020.1	3.408	2.186E−06
6	349.814	0.268	1,021.7	3.649	1.990E−06
7	347.526	0.246	1,023.2	4.051	1.813E−06
8	345.267	0.225	1,024.7	4.183	1.650E−06
9	343.038	0.206	1,026.2	4.498	1.501E−06
10	340.838	0.188	1,027.6	4.587	1.365E−06
11	338.667	0.172	1,029.0	4.630	1.242E−06
12	336.525	0.157	1,030.3	4.724	1.132E−06
13	334.413	0.144	1,031.6	4.777	1.030E−06
14	332.330	0.132	1,032.8	4.925	9.391E−07
15	330.276	0.120	1,034.0	5.015	8.543E−07
16	328.251	0.110	1,035.2	5.553	7.778E−07
17	326.255	0.101	1,036.4	5.923	7.086E−07
18	324.288	0.092	1,037.5	6.318	6.458E−07
19	322.351	0.085	1,038.5	6.637	5.896E−07
20	320.443	0.077	1,039.6	7.178	5.378E−07
21	318.564	0.071	1,040.5	7.628	4.910E−07
22	316.714	0.065	1,041.5	8.305	4.484E−07
23	314.894	0.060	1,042.4	8.612	4.107E−07
24	313.103	0.055	1,043.3	9.718	3.756E−07
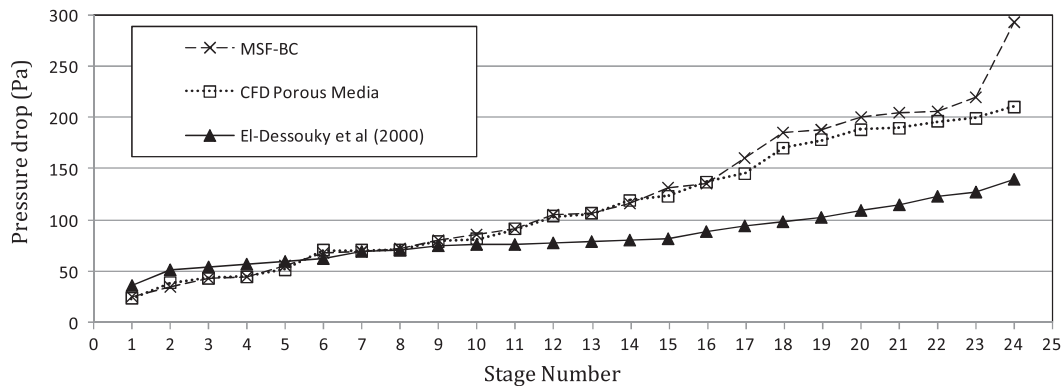
Fig. 4. Variation in pressure drop as a function of MSF-BC stage number for demister with packing density = 80.317 kg/m^3.

conditions and design parameters of the demister that were used as input values for the model.

As shown in Fig. 3, the comparison between the experimental data, CFD results, and empirical correlation values obtained by El-Dessouky et al. [2], which is applicable for the whole range of data, showed that the difference between the CFD results and the experimental data in all runs did not exceed 6%, whereas the difference between the empirical correlations exceeded 32%. Therefore, the CFD model is more accurate than the correlation predicted by El-Dessouky et al. [2].

Additionally, the CFD FLUENT code was used to simulate a wire mesh demister installed in an operating multistage flashing (MSF) desalination plant. The demister used in this plant had a packing
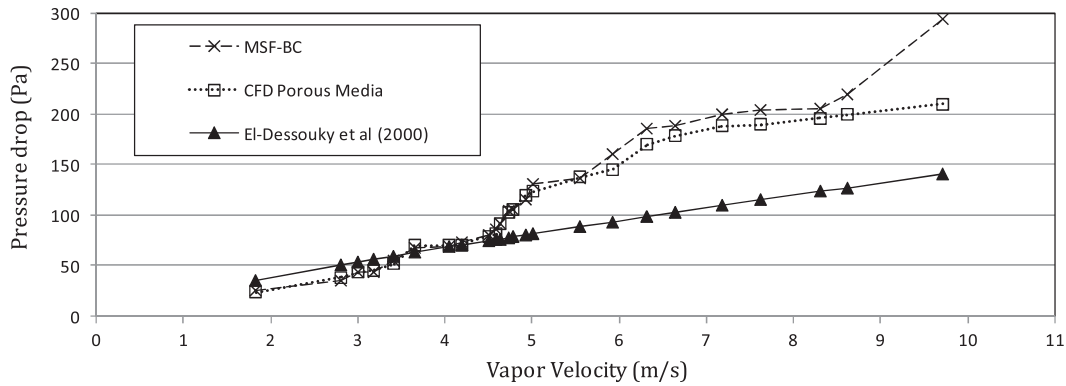
Fig. 5. Variation in pressure drop as a function of MSF-BC stage vapor velocity for demister with packing density = 80.317 kg/m³.
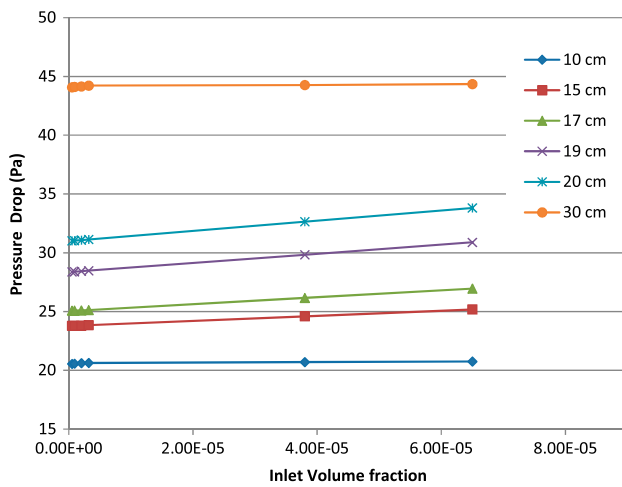
Fig. 6. Effect of flashed-off vapor composition on pressure drop across the demister at different demister heights.
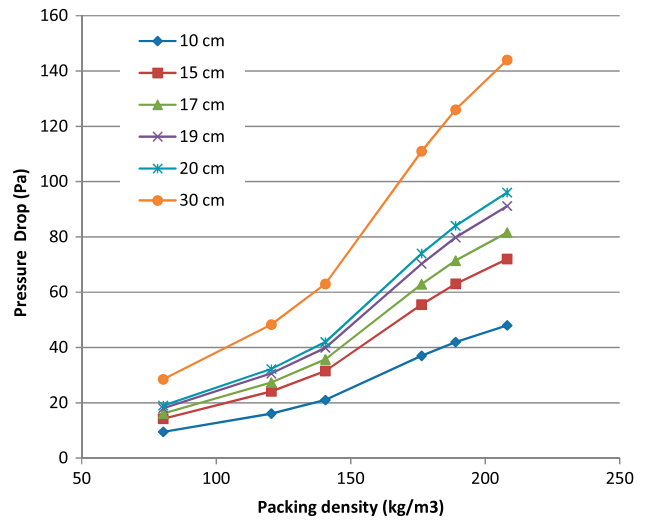
Fig. 7. Effect of the demister packing density on pressure drop across the demister for different demister heights.

density = 80.317 kg/m³ and 0.28-mm wire diameter. Table 3 includes the operating conditions for each flashing stage, which were used as input values in the simulator. Each flashing stage represents a separate simulation condition because it has its own set of operating conditions. This wide range of conditions makes the model more general and applicable for any demister installed in a plant.

The validation of porous media model is shown in Figs. 4 and 5. The predicted results of the model and the real MSF plant data were consistent. As shown, the relative error was less than 10%, except for the last two stages where the relative error reached 28%. The empirical correlation results were significantly different from the real MSF plant data with a relative error exceeding 52%.

It should be noted that a large increase in the pressure drop occurred in the last flashing stage. This was caused by the level controller of the last stage that maintains the brine height at a fixed value of 0.7 m. This decreased the free board distance between the demister and the surface of the brine. As a result, the entrainment rate of brine droplets significantly increased relative to the previous flashing stages, where the brine height is always less than 0.6 m. This effect was not included in the model, which used a linear entrainment rate for all flashing stages.

8. Pressure drop correlation

Next, the model was used to perform a sensitivity analysis to study the effect of various operating and
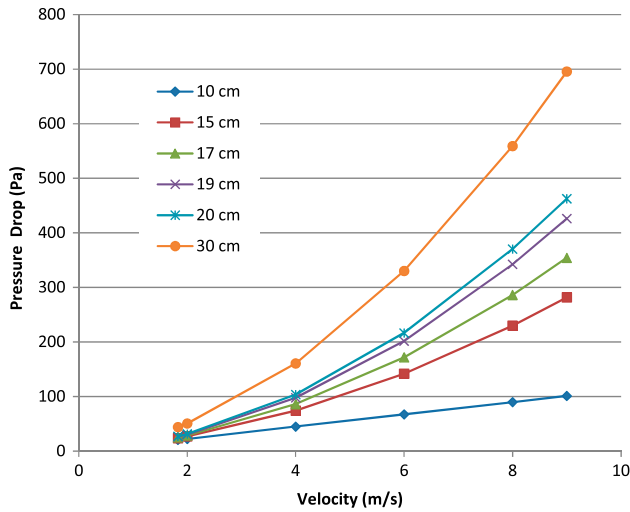
Fig. 8. Effect of flashed-off vapor velocity on pressure drop across the demister for different demister heights.

design parameters (packing density, flashed-off vapor velocity, flashed-off vapor composition, and demister height). As shown in Fig. 6, as the flashed-off vapor composition increases, the pressure drop increases slightly. This is because as the number of droplets in the vapor stream increases, more liquid accumulates in the demister until it settles down, which causes a resistance to the vapor flow and slightly increases the pressure drop. Also, it is shown that as the demister height increases, the pressure drop increases too.

As shown in Fig. 7, as the demister packing density increases, the pressure drop increases too. This is because as the demister packing density increases, the amount of resistant force applied to the flow increases, which results in a higher drop in pressure.

As shown in Fig. 8, as the flashed-off vapor velocity increases, the pressure drop increases. This is because the increase in the vapor velocity implies an increase in the amount of vapor flowing through the
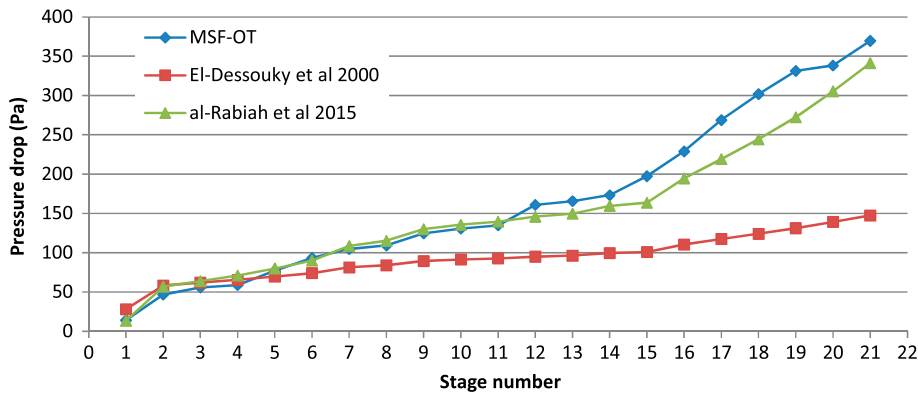
Fig. 9. Variation in pressure drop as a function of MSF stage number for demister with packing density 80.317 kg/m^3 in MSF-OT plant.
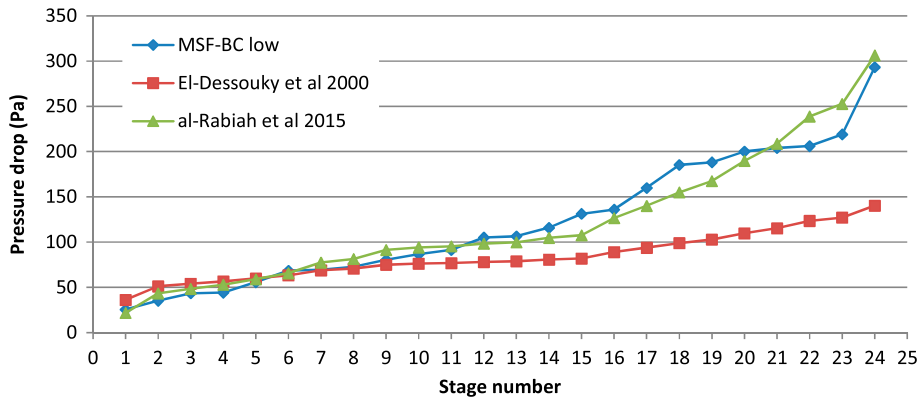
Fig. 10. Variation in pressure drop as a function of MSF stage number for demister with packing density 80.317 kg/m^3 in MSF-BC plant operating at low temperatures.
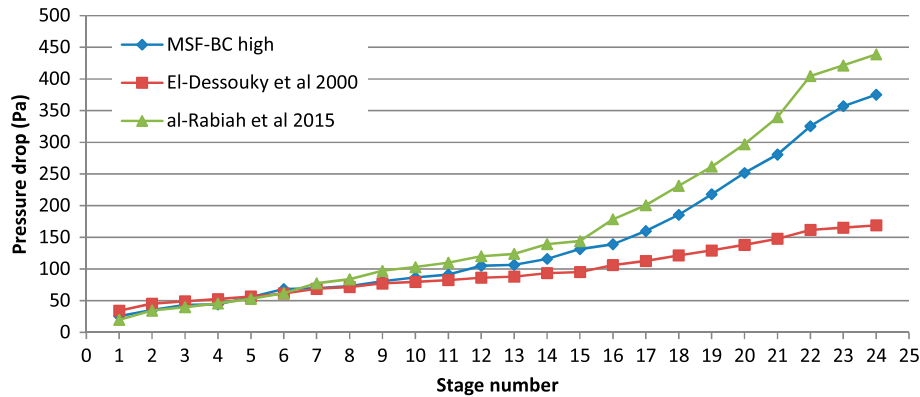
Fig. 11. Variation in pressure drop as a function of MSF stage number for demister with packing density 80.317 kg/m^3 in MSF-BC plant operating at high temperatures.

demister and since the void space for vapor is the same, the friction between the flowing vapor and demister wires increases and that causes an increase in the pressure drop across the demister.

The collected numerical data were used to develop the following correlation for the pressure drop across the demister as a function of the vapor velocity, the packing density, the demister length, and the inlet volume fraction of brine droplets:

$$\Delta P = 0.5317 V^{1.607} \rho_P^{1.1087} \psi_l^{0.02} L^{0.9827} \tag{30}$$

where V is the flashed-off vapor velocity and ranges between (1.2 and 12.5) m/s, ρ_P is the packing density and ranges between (80 and 209 kg/m^3), ψ_l is the inlet volume fraction of brine droplets and ranges between (4E−7 and 6.5E−6), and L is the demister height and ranges between (0.1 and 0.3 m). As shown in Figs. 9–11, the predicted correlation showed a good agreement with real plant data with an error less than 20%, while for El-Dessouky [2] correlation, the maximum error was almost 70%.

9. Conclusions

A CFD model for simulating the MSF demister was developed and evaluated. Next, a sensitivity analysis was done to determine the effect of some operating and design parameters on the pressure drop across the demister in the flashing stage. Finally, a new correlation was predicted for the pressure drop across the demister and compared against real plant data and other available correlation. This Eulerian–Eulerian CFD study is novel to the literature because it presents new data and analyses on the performance of the MSF demister as well as prediction of new

correlation. Porous media approach was used to model the demister based on the multiphase flow model. The model was simulated using the CFD software (FLUENT).

The Eulerian–Eulerian model was validated against real plant data and experimental data. The CFD predictions were consistent with the experimental/real plant data. The model validation was performed for both approaches and demonstrated that the CFD simulation results are more accurate than the available empirical correlation. A sensitivity analysis was performed to predict the effect of various operating/design variables on demister performance. That was followed by predicting a new correlation for the pressure drop across the demister and that was compared against real plant data and other available correlation. This model can be used to simulate and troubleshoot; also the new correlation can be used in any demister due to its wide range of variables which covers the real plant operating and design conditions. This will help in the further design of other parts of the MSF flashing stage such as the condenser area. However, it cannot be used toward the design of new demisters because the model requires prior knowledge of the demister separation efficiency to set the sink value, which is not known when designing a new demister and should be evaluated.

Nomenclature

A_{do}	—	total projected area of droplets in a given control volume (m^2)
C_1	—	constant in k–ε model
C_2	—	constant in k–ε model
C_f	—	interfacial friction coefficient
C_μ	—	constant in k–ε model
D_{ot}	—	outer diameter of the demister wires (mm)

f	—	friction factor
f_d	—	friction factor
g	—	gravity acceleration (m/s^2)
k	—	turbulent kinetic energy (m^2/s^2)
$\dot{m}$	—	mass rate of collected liquid droplets per unit volume (kg/s m^3)
P	—	pressure (kPa)
P_t	—	tube pitch (m)
ΔP	—	pressure drop between stages (Pa)
ΔP_p	—	demister pressure drop (Pa)
Re	—	Reynolds number
R	—	source term due to tube bundles
S	—	source term due to interfacial friction
t	—	time (s)
U	—	overall heat transfer coefficient (kW/m^2°C)
U_g	—	vapor velocity magnitude $= \left(u^2 + v^2\right)^{0.5}$ (m/s)
U_l	—	liquid velocity magnitude $= \left(u^2 + v^2\right)^{0.5}$ (m/s)
u	—	velocity component in the x-direction (m/s)
V	—	volume (m^3)
$\vec{v}$	—	velocity vector
v	_	velocity component in the y-direction (m/s)

Greek letters

ε	—	turbulent dissipation rate
ρ	—	mass density (kg/m^3)
ψ	—	volume fraction
ω	—	local porosity
ω_{td}	—	tube bundle porosity
τ	—	shear stress (Pa)
δ	—	permeability (m^2)
μ	—	laminar dynamic viscosity (cp)
μ_t	—	turbulent viscosity (cp)
μ_{eg}	—	effective viscosity (cp)
$\sigma_k, \ \sigma_\varepsilon$	—	constants

Subscripts

g	—	gas phase (vapor water)
l	—	liquid phase (entrained liquid droplets)
x	—	x coordinate
y	—	y coordinate
p	—	packing
w	—	wire

References

[1] E. Hawaidi, I. Mujtaba, Effect of demister separation efficiency on the freshwater purity in MSF desalination process, Comput. Aided Chem. Eng. 29 (2011) 1180–1184.

[2] H.T. El-Dessouky, I.M. Alatiqi, H.M. Ettouney, N.S. Al-Deffeeri, Performance of wire mesh mist eliminator, Chem. Eng. Process. 39 (2000) 129–139.

[3] A. Buerkholz, Droplet Separation, VCH, New York, NY, 1989.

[4] H. Ettouney, Brine entrainment in multistage flash desalination, Desalination 182 (2005) 87–97.

[5] J. Gharib, M.K. Moraveji, Determination the factors affecting the vane-plate demisters efficiency using CFD modeling, J. Chem. Eng. Process. Technol. S1 (2012) 1–5, doi: 10.4172/2157-7048.S1-003.

[6] G. Venkatesan, N. Kulasekharan, S. Iniyan, Influence of turbulence models on the performance prediction of flow through curved vane demisters, Desalination 329 (2013) 19–28.

[7] G. Venkatesan, N. Kulasekharan, S. Iniyan, Numerical analysis of curved vane demisters in estimating water droplet separation efficiency, Desalination 339 (2014) 40–53.

[8] G. Venkatesan, N. Kulasekharan, S. Iniyan, (2014). Design and selection of curved vane demisters using Taguchi based CFD analysis, Desalination 354 (2014) 39–52.

[9] H. Al-Fulaij, A. Cipollina, G. Micale, D. Bogle, H. Ettouney, CFD modelling of the demister in the multi stage flash desalination plant, Comput. Aided Chem. Eng. 29 (2011) 1618–1622.

[10] R. Rahimi, D. Abbaspour, Determination of pressure drop in wire mesh mist eliminator by CFD, Chem. Eng. Process. 47 (2008) 1504–1508.

[11] C. Galletti, E. Brunazzi, L. Tognotti, A numerical model for gas flow and droplet motion in wave-plate mist eliminators with drainage channels, Chem. Eng. Sci. 63 (2008) 5639–5652.

[12] J. Zhao, B. Jin, Z. Zhong, Study of the separation efficiency of a demister vane with response surface methodology, J. Hazard. Mater. 147 (2007) 363–369.

[13] R. Kouhikamali, S.M.A. Noori Rahim Abadi, M. Hassani, Numerical study of performance of wire mesh mist eliminator, Appl. Therm. Eng. 67 (2014) 214–222.

[14] H. Al-Fulaij, A. Cipollina, G. Micale, H. Ettouney, D. Bogle, Eulerian–Eulerian modelling and computational fluid dynamics simulation of wire mesh demisters in MSF plants, Eng. Comput. 31 (2014) 1242–1260.

[15] F.Ronald Probstein, Physicochemical Hydrodynamics An Introduction, Butterworth Publishers, USA, 1989.

[16] O.Zikanov, Essential Computational Fluid Dynamics, Wiley, New Jersey, 2010.

[17] H.G. Hu, C.A. Zhang, A modified k–ε turbulence model for the simulation of two-phase flow and heat transfer in condensers, Int. J. Heat Mass Transfer 50 (2007) 1641–1648.

[18] H.F.Al-Fulaij, Dynamic Modeling of Multi Stage Flash (MSF) Desalination Plant, PhD Thesis, University College London (UCL), United Kingdom, 2011.

[19] C. Zhang, A. Bokil, A quasi-three dimensional approach to simulate the two-phase fluid flow and heat transfer in condensers, Int. J. Heat Mass Transfer 40 (1997) 3537–3546.

[20] R. Clift, J.R. Grace, M.E. Weber, Bubbles, Drops and Particles, Academic Press, New York, NY, 1978.

[21] D.B. Rhodes, L.N. Carlucci, Predicted and measured velocity distribution in a model heat exchanger, International Conference on Numerical Methods in Nuclear Engineering, Canadian Nuclear Society– American Nuclear Society, Montreal, 1983.

[22] Fluent_Inc. Fluent 6.3 Manual, Fluent Inc, Centerra Resource Park, 2006.
[23] S. Ergun, Fluid flow through packed column, Chem. Eng. Prog. 49 (1952) 89–94.
[24] L. Mazzei, A. Casillo, P. Lettieri, P. Salatino, CFD simulations of segregating fluidized bidisperse mixtures of particles differing in size, Chem. Eng. J. 156 (2010) 432–445.
[25] E. Brunazzi, A. Paglianti, Design of wire mesh mist eliminators, AIChE J. 44 (1998) 505–512.
[26] N. Al-Deffeeri, Chemical Section Head, Doha West Power Station, Ministry of Water and Electricity, Kuwait, Personal Communication, 2009.